Universiteit Antwerpen

This item is the archived peer-reviewed author-version of:

3D atomic-scale dynamics of laser-light-induced restructuring of nanoparticles unraveled by electron tomography

Reference:
Albrecht Wiebke, Arslan Irmak Ece, Altantzis Thomas, Pedrazo-Tardajos Adrián, Skorikov Alexander, Deng Tian-Song, van der Hoeven Jessi E.S., van Blaaderen Alfons, Van Aert Sandra, Bals Sara.- 3D atomic-scale dynamics of laser-light-induced restructuring of nanoparticles unraveled by electron tomography
Advanced materials - ISSN 0935-9648 - Weinheim, Wiley-v c h verlag gmbh, 33:33(2021), 2100972
Full text (Publisher's DOI): https://doi.org/10.1002/ADMA.202100972
To cite this reference: https://hdl.handle.net/10067/1797810151162165141

uantwerpen.be
Institutional repository IRUA

Three-Dimensional Atomic Scale Dynamics of Laser Light Induced Restructuring of Nanoparticles Unraveled by Electron Tomography

Wiebke Albrecht Ece Arslan Irmak Thomas Altantzis Adrián Pedrazo-Tardajos Alexander Skorikov Tian-Song Deng Jessi E.S. van der Hoeven Alfons van Blaaderen* Sandra Van Aert* Sara Bals**

Dr. W. Albrecht, E. Arslan Irmak, Prof. Dr. T. Altantzis, A. Pedrazo-Tardajos, A. Skorikov, Prof. Dr. S. Van Aert, Prof. Dr. S. Bals
EMAT and NANOlab Center of Excellence, University of Antwerp, Groenenborgerlaan 171, B-2020 Antwerp, Belgium
Email Address: wiebke.albrecht@uantwerpen.be; sandra.vanaert@uantwerpen.be; sara.bals@uantwerpen.be
Dr. T.-S. Deng
School of Electronics and Information Engineering, Hangzhou Dianzi University, No. 1158, 2nd Avenue, Baiyang Street, Hangzhou 310018, China
Dr. W. Albrecht, Dr. J. E. S. van der Hoeven, Prof. Dr. A. van Blaaderen
Soft Condensed Matter, Debye Institute for Nanomaterials Science, Utrecht University, Princetonplein 5, 3584 CC Utrecht, The Netherlands
Email Address: a.vanblaaderen@uu.nl

Keywords: *atomic resolution electron tomography, femtosecond laser excitation, gold nanorods, reshaping, molecular dynamics simulations*

Understanding light-matter interactions in nanomaterials is crucial for optoelectronic, photonic and plasmonic applications. Specifically, metal nanoparticles strongly interact with light and can undergo shape transformations, fragmentation and ablation upon (pulsed) laser excitation. Despite being vital for technological applications, experimental insight into the underlying atomistic processes is still lacking due to the complexity of such measurements. Herein, atomic resolution electron tomography on the same mesoporous silica-coated gold nanorod, before and after femtosecond laser irradiation, is performed to assess the missing information. Combined with molecular dynamics simulations based on the experimentally determined three-dimensional atomic scale morphology, the complex atomistic rearrangements, causing shape deformations and defect generation are unraveled. These rearrangements are simultaneously driven by surface diffusion, facet restructuring and strain formation, and are influenced by subtleties in the atomic distribution at the surface.

The interaction of metal nanoparticles (NPs) with ultrashort laser pulses has been an intensive research topic due to their unique optical and photothermal properties, which led to numerous applications in, amongst others, biomedicine, [1, 2] sensing, [3, 4, 5] imaging, [6, 7] data storage [8, 9, 10] and catalysis. [11, 12, 13] These properties stem from the efficient interaction of metal NPs with light via localized surface plasmon resonances (LSPRs). Specifically, the electronic absorption of the laser energy and subsequent electron-phonon scattering heats up the NP's crystal lattice, possibly leading to atomic restructuring. [14, 15, 16, 17] This reshaping depends on the laser pulse width, [18] fluence [15, 17, 19] and repetition rate. [20] Excitation with femtosecond laser pulses generally results in more uniform reshaping of anisotropic NPs, whereas nanosecond pulses are likely to induce fragmentation and irregular morphologies. [18]

Next to the above-mentioned factors, the NP's environment plays a pivotal role due to possible hindrance of surface atom diffusion and its effect on heat dissipation. [19, 21, 22, 23, 24, 25] To improve the robustness and durability in applications, surface coating of nanoparticles was investigated, with silica-coated Au NPs emerging as one of the most well-suited systems in practice. [26, 27] For biomedical applications, for example, silica coatings were shown to provide biocompatibility, large surface areas for drug delivery and prevent aggregation of NPs inside cells. [28] Next to their increased colloidal and thermal stability, silica-coated Au NPs also exhibited superior performance for imaging applications such as photoacoustic imaging [29] and a higher dynamic range for optical data storage. [30] In the case of catalytic applications, porous silica coatings provide accessibility to the NP's surface while inhibiting sintering, [31, 32] which is one of the main deactivation channels of catalytic metal NPs.

Despite their relevance in applications, not much is known about the atomistic processes occuring in (porous) silica coated Au NRs when exposed to high temperatures or laser irradiation as most work so

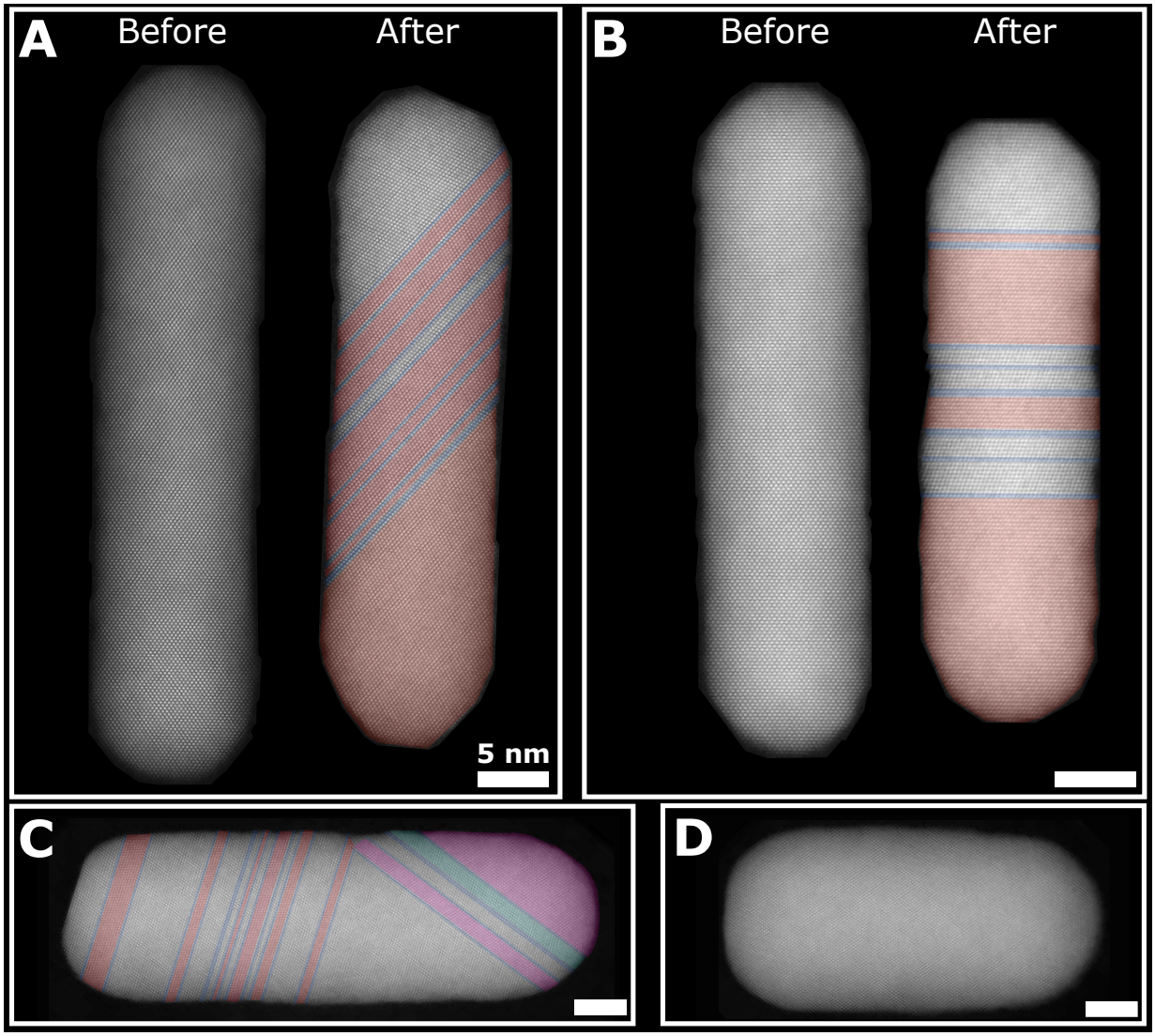

Figure 1: Defect creation upon femtosecond laser excitation. A) High-resolution HAADF-STEM images of the same mesoporous silica coated Au NR before and after laser excitation with an initial length and width of 51.2 nm and 11.6 nm, respectively. Upon laser excitation the AR of the NR decreased from 4.4 to 3.8 and twinning planes appeared. B) High-resolution HAADF-STEM images of another mesoporous silica coated Au NR before and after laser excitation with an initial length and width of 40.9 nm and 9.6 nm, respectively. Similarly to the NR in (A), the AR decreased from 4.3 to 3.5 and twinning planes occurred after laser irradiation. C) and D) show examples of other silica-coated Au NRs of the same sample batch after laser excitation (under the same conditions) and oven heating at 500°C for 2 h, respectively. In contrast to laser-heating, the latter led to defect-free reshaping. The colours in (A)-(C) correspond to different crystal orientations. The deformed NRs in (A)-(C) were excited at 925 nm with a fluence of 6.5 mJ/cm^2. It should be noted that although the silica coating is surrounding the NRs, it is not visible in the HAADF-STEM images due to the large contrast difference between silica and gold. All scale bars represent 5 nm.

far has focused on bare Au NPs. For uncoated NRs, surface atom diffusion is believed to be the driving mechanism of photothermal reshaping for absorbed energies below the melting energy, [16] but internal crystal defects in irradiated NPs have also been reported. [33, 17] Matsumura and co-workers observed twinning and different crystallographic orientations in initially single-crystalline and defect-free gold nanorods (NRs) upon excitation with nanosecond laser pulses. [34] Several molecular dynamics (MD) studies reported the creation of stacking faults, which originated at the NP surface upon heating. [35, 36] Moreover, more accurate modeling of laser heating of a Au NR revealed that surface pre-melting predominantly occurred at {110} lattice planes and started before the creation of parallel twin boundaries, appearing in the middle of the NR. [37]
Unfortunately, accessible time and length scales are generally different between experiments and simu-

lations. Most experimental work to understand photothermal reshaping has been performed at the ensemble level using optical techniques. Although optical single-particle studies gained additional insight on this mechanism, [15, 16] few reports exist on structural changes of excited NPs. Such studies were mainly performed by scanning electron microscopy (SEM) [15, 16] or transmission electron microscopy (TEM) at medium spatial resolution and via observing two-dimensional (2D) projections of the three-dimensional (3D) NP. [22, 34, 38] On the other hand, simulation studies are generally performed at the single particle level using short time and atomic spatial scales. A complete picture of the reshaping and defect formation mechanism, combining experiments and simulations, is still lacking. Here, we bridge the gap between simulations and experiments by performing atomic resolution electron tomography of the same mesoporous silica-coated Au NR before and after femtosecond laser excitation. The experiments enabled us to perform MD simulations using the experimentally determined morphology, thereby extending previous simulation studies to an experimental system with realistic surface morphologies.

To understand the impact of the absorbed laser energy on the structure and morphology, we imaged the same Au NRs before and after multi-shot fs laser excitation at their ensemble-average longitudinal plasmon resonance. Hereby, the NRs were deposited on a TEM grid. For bare NRs, however, this leads to symmetry breaking and hindered deformation of the NR side touching the support. A mesoporous silica coating around the Au NRs, on the other hand, guarantees a homogenous surrounding, while enhancing the thermal stability of Au NRs. [19, 22] We focused on the early stages of below-melting-point deformation as these contain most information about the interplay between structural and morphological changes. Furthermore, below-melting-point deformation is highly relevant for applications since it can e.g. be used to shape or weld NPs into desired configurations. [24, 39] Consequently, we selected a laser fluence that induced only mild NR reshaping (see 'Femtosecond laser excitation' in supplementary materials).

Figure 1A,B shows atomic resolution high-angle annular dark-field scanning TEM (HAADF-STEM) images of two silica-coated NRs before and after laser excitation (more examples in Figure S6). The NRs were defect-free before laser excitation and contained lattice defects and a decreased aspect ratio (AR) afterwards. It is interesting to note the connection between NR deformation and defect occurrence. Indeed, NRs without any morphological changes after laser excitation, appeared to be defect-free (arrow in Figure S6). Mostly, twin boundaries were observed and for the majority of the investigated NRs, these were perfectly parallel (Figure 1A,B). However, Figure 1C suggests that under the same irradiation conditions twin boundaries were also found along more than one direction.

The occurrence of defects was observed for a large range of particle volumes. Silica-coated NRs with as much as an order of magnitude difference in volume ($9.6\cdot 10^4\,\mathrm{nm}^3$ vs $1.1\cdot 10^4\,\mathrm{nm}^3$) developed similar lattice defects (Figure S7). Defects also appeared for NRs without a silica shell (Figure S8), in addition to irregular, asymmetric shapes and volume loss. We believe that the irregularity in shapes for uncoated NRs mainly stems from non-uniform properties of their environment, specifically its rigidity and heat conductivity, which are influenced by the contact with the TEM support, which is prevented by the silica shell. [22] This effect was most likely hidden in previous correlative SEM experiments on glass substrates yielding lower spatial resolutions than TEM. [15, 16]

In addition to twinning boundaries, the deformed NRs in Figure 1A-C show a bullet-like intermediate shape, as was also previously observed for silica-coated Au NRs after femtosecond laser excitation. [22] For uncoated NRs, a similar deformation occurred for some Au NRs (Figure S8) but due to the aforementioned symmetry breaking, most NRs deformed into irregular shapes. Interestingly, almost all silica-coated Au NRs did not show crystal defects when heated in a furnace (examples in Figure 1D and S9). Moreover, the silica-coated Au NRs did not fully transform into a spherical shape under these conditions, as expected for as-synthesized Au NRs without a silica shell. [40] This is due to the hindrance of surface atoms induced by the silica confinement.

For all of these observations, however, caution needs to be taken when interpreting the shape of a 3D object from 2D projection images. To unambiguously determine the 3D morphology and to understand the role of crystal facets during reshaping, a 3D analysis is indispensable. Hence, we acquired an atomic resolution electron tomography tilt series before and after laser excitation for the NR of Figure 1A (see

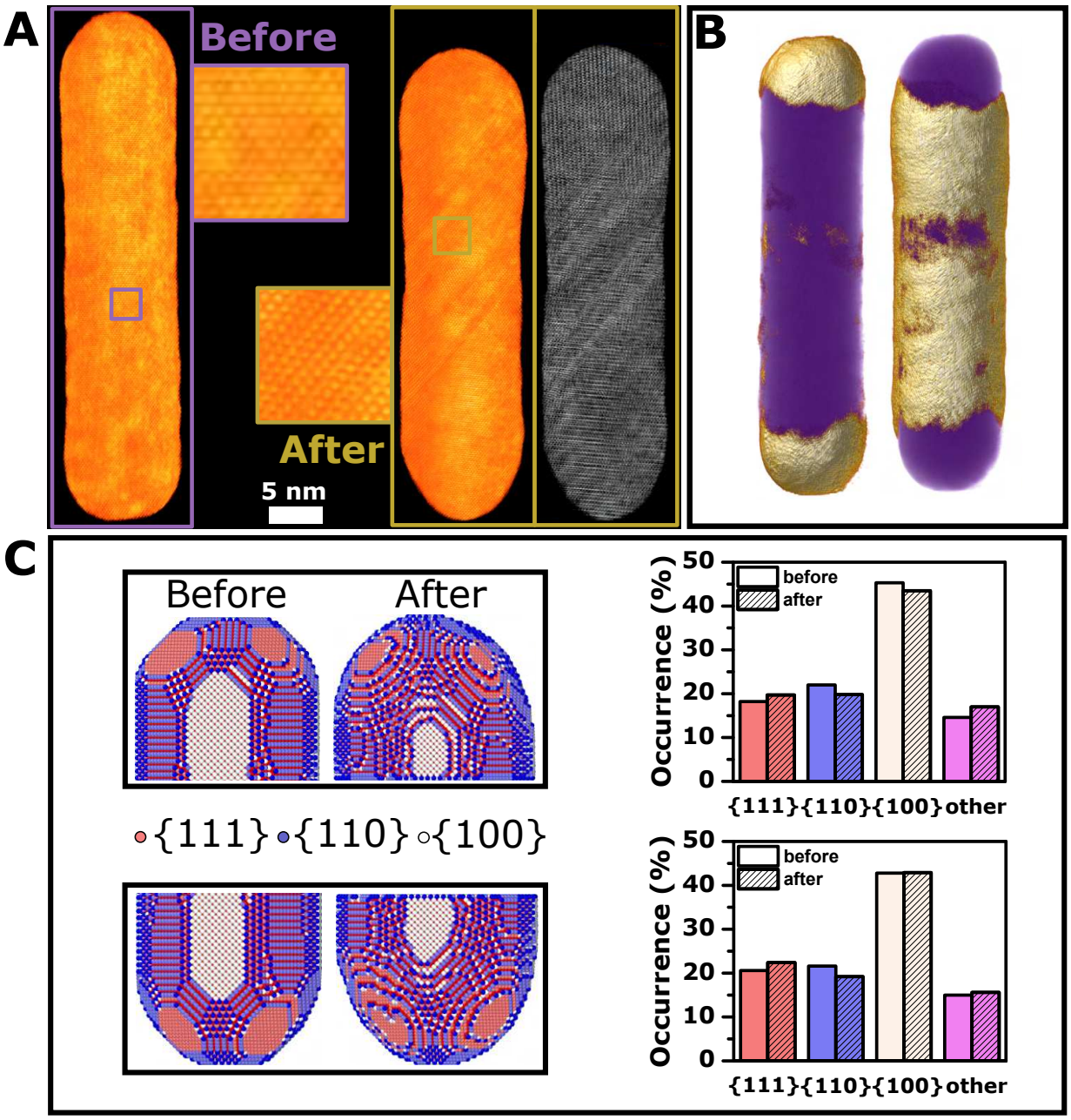

Figure 2: Atomic resolution tomography of the same silica coated Au NR before and after femtosecond laser excitation (silica not shown). A) 3D visualization of the reconstructed Au NR before and after excitation with multiple femtosecond laser shots (925 nm, 6.5 mJ/cm^2) along the same viewing direction. A magnified visualization shows the single-crystalline nature of the particle before laser excitation. After excitation a magnified visualization and a slice through the middle of the NR (right box) confirm twinning defects. B) 3D visualization of redistributed volume upon laser excitation. The left and right sides show areas of local volume decrease and increase, respectively, overlaid on visualization of the segmented original NR (purple). C) Visualization and quantification of the facet distribution at the two tips before and after laser excitation.

supplementary materials for details). The 3D visualization of the reconstructions and corresponding slices through the NR volume are presented in **Figure 2**A and S10.

As expected, prior to laser excitation, the Au NR yielded a defect-free face-centered cubic (FCC) lattice with 35% {100}, 22% {110} and 20% {111} as well as higher order surface facets, without significant surface roughness (Figure 2A left side). After exposure to about 10^4 fs laser pulses (see 'Femtosecond laser excitation' in supplementary materials), the NR's surface roughened (Figure 2A right side) along with the appearance of twin boundaries. The latter extended throughout the whole NR (right side Figure 2A) and were parallel to the [111] viewing direction (Figure S10C), which is common for FCC lat-

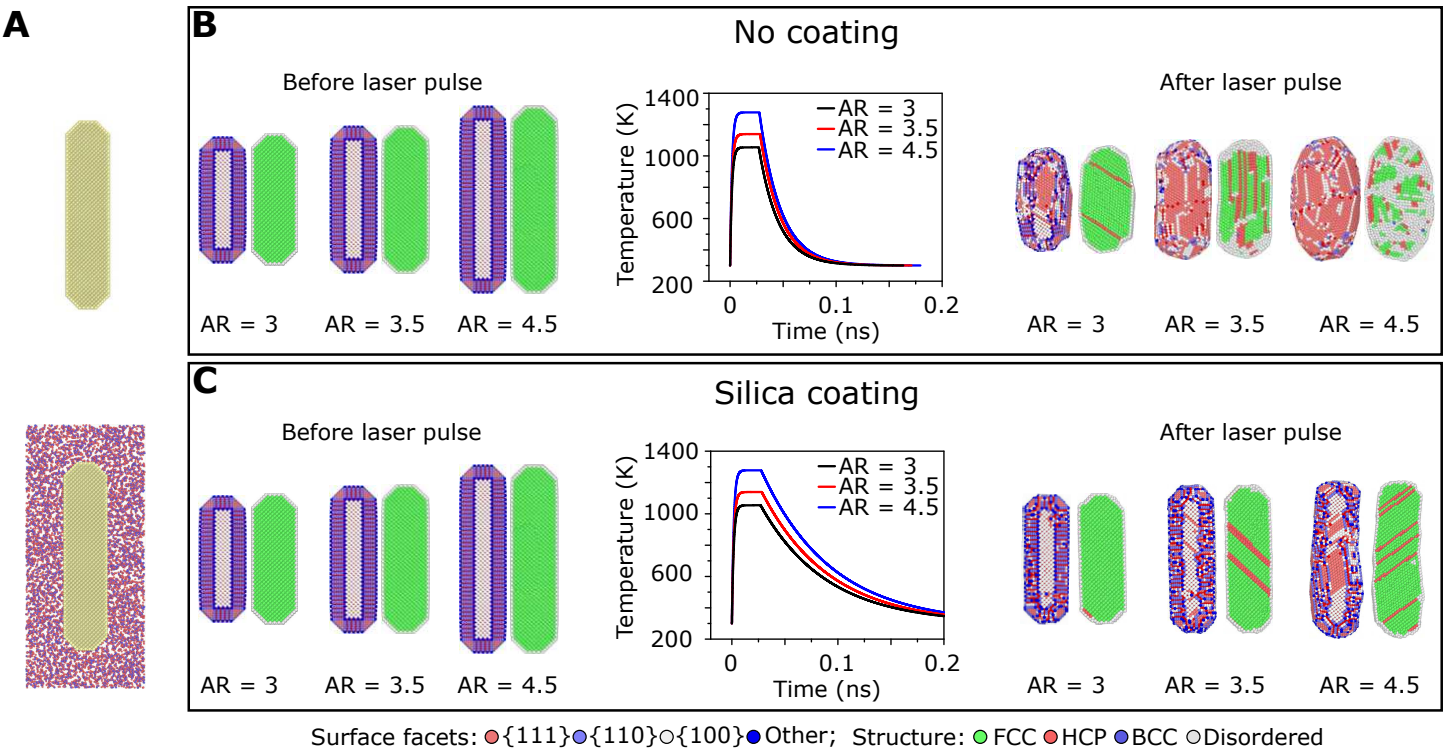

Figure 3: MD simulations of laser-heated gold nanorods with a model-like input structure. A) Cut through the input structures. B) Side views (left sides) and interior structure (right sides) before and after simulated laser pulse excitation and the calculated temperature profile for three different bare Au NRs with varying ARs. C) Side views (left sides) and interior structure (right sides) before and after simulated laser pulse excitation and the calculated temperature profiles for three different mesoporous silica-coated Au NRs with varying ARs. The silica coating is omitted in the visualizations.

tices. Because we extracted the 3D information of the same NR before and after laser excitation, we could calculate the redistributed volume, displayed in Figure 2B. The overall volume of the NR was 5.16 $\cdot$ 10^3 nm^3 and did not change after laser excitation. 9% of the NR's volume redistributed upon laser excitation. During this redistribution, about 28000 atoms diffused from the tips of the NR (left image in Figure 2B) to its side (right image in Figure 2B). This redistribution did not only lead to the observed AR reduction but also to facet restructuring (Figure 2C), where the more stable {111} surface facets expanded at the expense of less stable {100} and {110} facets.

To understand the mechanism of processes commencing upon laser excitation, we performed molecular dynamics simulations. Hereby, a representative heating regime for the laser irradiation is crucial because the structural changes induced in the gold nanorod depend on the heating rates [35] and the maximum temperature that is reached. To mimic the experiments, we developed a numerical calculation (see 'Heating regime of the femtosecond laser simulations' in supplementary materials). Importantly, we specifically included the cooling dynamics to simulate a complete laser pulse. In contrast to previous studies, the coating effect was also investigated by creating a realistic mesoporous silica coating (Figure S3). [41] We first compared the effect of the silica coating on the deformation for NRs with a diameter of 4 nm and three different ARs (3, 3.5 and 4.5). We used a model-like facet distribution as typically applied for MD simulations (**Figure 3**A). Side views and interior structure of the NRs before and after the modeled laser excitation as well as the temperature profile from the MD simulations are shown in Figure 3B,C. Visualizations at intermediate temperatures can be found in Figure S11 and S12. According to the calculated temperature profiles of the laser irradiation, the maximum temperature that the NR reached during laser heating increased with increasing AR and volume, in agreement with the shape-dependent plasmonic properties (Figure S4). The heat dissipation was slower for silica-coated NRs due to the additional heat resistance at the surface. The latter indicates the crucial importance of including the cooling process in the simulations.

Figure 3 shows that the silica coating improved the stability of the NRs (see also Figure S13A and S14).

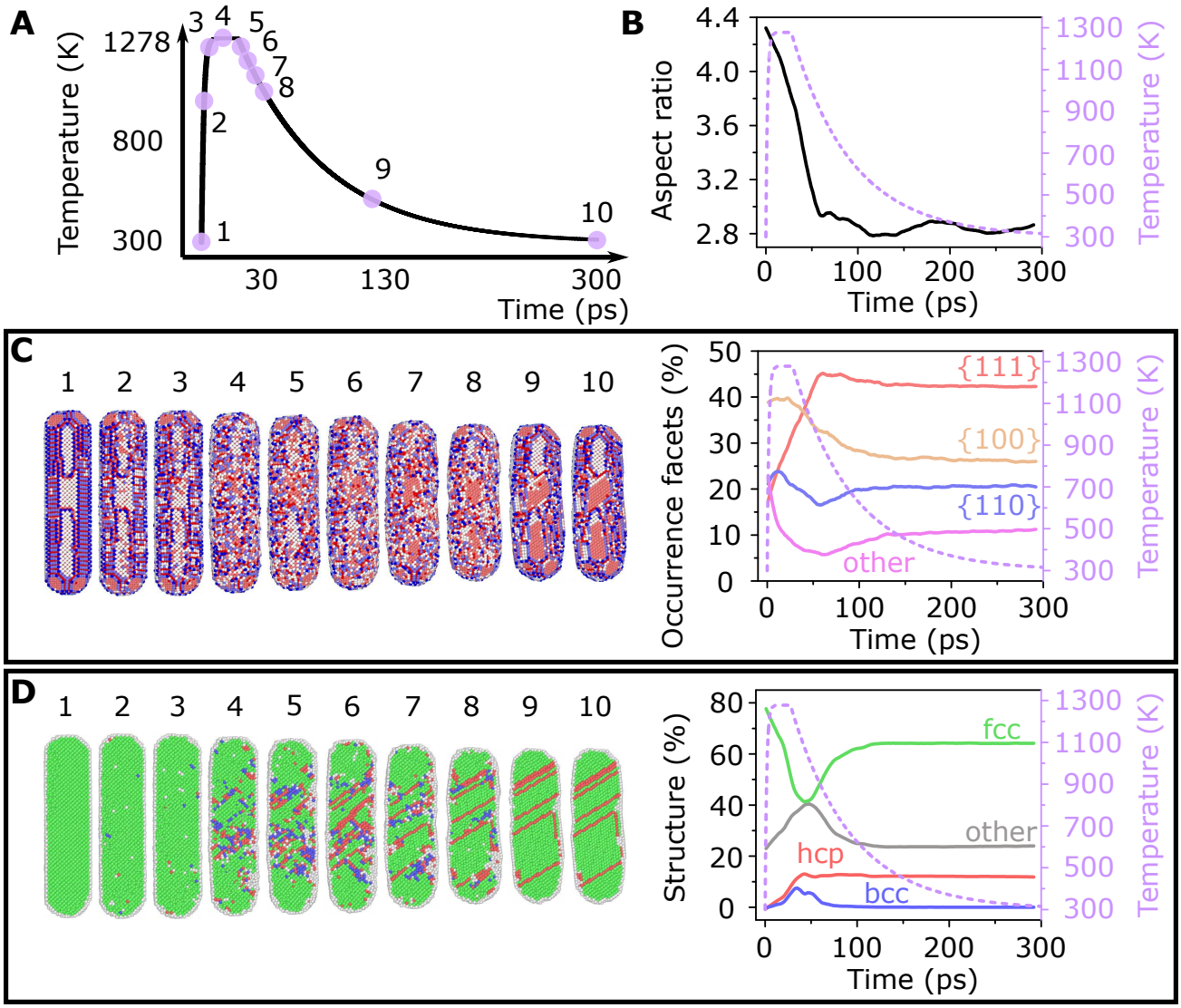

Figure 4: MD simulations for a mesoporous silica-coated Au NR with the experimentally measured surface facets as input structure (silica not shown). A) Applied laser heating profile (same as blue curve in Fig. 3B, B) AR change overlaid with the heating profile, C) side views at the time points indicated in a) and quantification of corresponding facet changes. D) Internal structure at the time points indicated in a) and quantification of structural changes. All colours in the graphs correspond to the same colours in the visualizations.

For the uncoated NRs, the ARs decreased by 34%, 36% and 56% for initial ARs of 3.0, 3.5 and 4.5, respectively. For the coated Au NRs the AR changes were smaller with 0%, 5% and 24%, respectively. The stronger deformation at larger ARs in the simulation can be attributed to the higher maximum heating temperature (Figure 3B,C) and the higher instability of larger AR NRs (Figure S15). We also found that the density of twinning planes after laser excitation differed according to the initial AR and the presence of a coating (Figure S14C). Hereby, the twin density increased with increasing AR (red atoms in Figure 3). Moreover, the effect of the silica coating resulted in the development of a multiple parallel twin structure, whereas for uncoated particles a range of defects, e.g. stacking faults and twinning planes, along the long axis of the NR were also observed. These observations are in excellent agreement with the experiments as we observed a higher density of twinning planes for higher AR samples (Figure S6 and S7) and parallel twin planes for the coated NRs (Figure 1 and 2). In addition, depending on the NR orientation, the twinning planes seemed to occur along seemingly different crystallographic directions (Figure S12), as observed in the experiments as well (Figure 1B,C).
The main benefit of the simulations comes from the ability to capture dynamic information of the underlying processes, which is presently impossible to assess experimentally. To shed light on the shape de-

formation dynamics of the experimental NRs, we directly used the information from atomic resolution electron tomography to construct an input structure that resembled the experimental NR more accurately than the model-like systems (see 'Creating input models' in supplementary materials and Figure S1). [36, 35, 37] This approach is unique and highly important as it enabled us to perform simulations based on the experimentally measured surface facets, the distribution of which is tremendously important for nanoscale processes. To compare with the model-like input structure of the coated 4.5-AR Au NR (Figure 3C), we scaled down the experimentally-based input structure to the same diameter of 4 nm and used the same heating profile (**Figure 4**A). The latter is applicable since the volume and AR of the two NRs are very similar. The main difference between the experimental-based and the model-like structure is the facet distribution (Figure S2). The rescaled experimental input structure contained a larger amount of {111} facets (18.3% compared to 3.4%) and a smaller amount of {100} and {110} facets. Upon laser heating, the shape transformation started almost immediately by a drop in the AR (Figure 4B), which did not change anymore during the rest of the cooling. In addition, this transformation was accompanied by an increase in {111} and decrease in lower coordinated facets (Figure 4C) as well as by internal restructuring from pure FCC to FCC with twinning planes (Figure 4D), in excellent agreement with experiments. Around 1024 K (point 2) hexagonal close-packed (HCP) and body-centered cubic (BCC) interior regions occurred within the FCC structure. Afterwards, the percentage of HCP and BCC atoms and {111} facets increased continuously (point 3). Upon reaching the maximum temperature (point 4), the growth of the HCP structure resulted in stacking faults that concentrated in the middle of the NR. Disordering continued until the NR cooled down to about 1150 K (point 7), when the minimum of internal FCC structure was reached. During cooling, the distance between the twin planes increased while surface reorganization continued until 500 K (point 9). The slower heat dissipation for coated NRs, compared to uncoated NRs, resulted in more time for the HCP internal regions to grow into twinning. We could experimentally confirm that the ordering into multiple twins occurred after surface diffusion as twins extended over multiple NPs which welded together upon laser excitation (Figure S16). To evaluate whether the internal lattice defects were caused by induced strain due to the surface transformation, we performed atomic strain analysis (**Figure 5**A). Figure 5B connects the change in AR, shear strain, occurrence of {111} surface facets and HCP internal transformation. At the beginning of laser heating, the shear strain increased almost instantaneously due to the displacement of atoms out of their equilibrium position (magenta arrow in Figure 5B). The onset of surface diffusion was reflected in the increase in {111} surface facets and change in AR. Simultaneously, the first HCP interior atoms appeared prior to localized melting in accordance with literature. [17] Until the maximum temperature was reached (point 4 in Figure 5A), internal strain was only related to displaced atoms due to heating. Then, localized stress propagated from the surface through the internal structure (white arrows in Figure 5A). Together with localized melting around the interior areas with HCP and BCC defects occuring around point 4 (Figure S17), internal planes shifted, forming stacking faults in the middle of the NR. During cooling at 1080 K (around point 8) the HCP percentage reached its maximum. The change in AR and {111} facets was maximal at around 900 K, while the shear strain continued to slowly increase until around 660 K, causing the separation of neighbouring stacking fault HCP layers, which resulted in multi-twin boundaries.

Although the final morphology of the model-like (Figure 3) and the experimental (Figure 4) input structure appear qualitatively similar (**Figure 6**A), quantitative differences exist. The NR based on the experimental input facets was less stable as evident from the larger change in AR (Figure 6B) and although the transformation of the internal structure was almost identical (Figure 6C), the relative facet changes differed significantly. The relative {111} facet transformation occurred faster for the model-like input structure in the initial stage and also an additional 10% of the surface facets were transformed into {111} facets (Figure 6D) compared to the experimental input structure. This observation clearly shows the importance of using experimental structures as input for simulations. Moreover, it demonstrates that morphology-dependent surface diffusion and facet restructuring simultaneously drive the deformation of metal NPs.

From a thermodynamics point of view, all anisotropic Au NPs are unstable or far out of equilibrium and

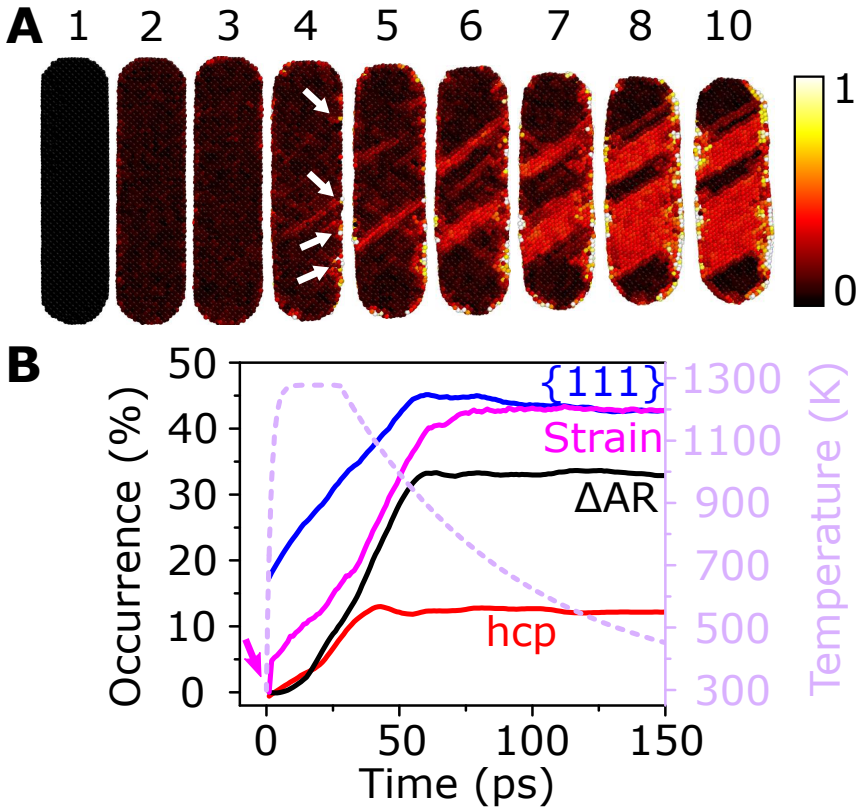

Figure 5: Strain analysis of the simulated silica-coated Au NR in Fig. 4. A) Atomic shear strain maps taken at the same time points as in Fig. 4. The atoms are coloured according to their local shear strain, which is measured by the displacement gradient of atoms with respect to their initial positions and taking into account the relative displacements of the neighbouring atoms. B) Comparison of strain, AR change, {111} facet evolution and HCP atoms occurrence.

will strive to reach an equilibrium shape. According to the Wulff theorem, the equilibrium shape of our Au NPs is a truncated octahedron exposing {100} and {111} facets. [42] On the other hand, surface coatings can kinetically stabilize an out-of-equilibrium shape, at least at room temperature. At elevated temperatures, these kinetic barriers can be overcome and the particles will transform towards their thermodynamically stable shapes. Two critical parameters of this transformation process are heating temperature and time. [40, 22, 17] For heating temperatures above the melting point, the NP will melt and recrystallize into its thermodynamically stable shape. For laser-heated NRs, the heating time and the achievable deformation is limited. [40] Allowing the NR more time to reach its thermodynamically stable state, led to a stronger deformation despite lower (Figure 1D) or the same maximum heating temperature (Figure S13A and S18).

As demonstrated above, the NR did not only lower its AR but also developed multiple twin boundaries after laser illumination. Concerning the atomistic mechanism in creating lattice defects, our results bridge different studies in literature. On the one hand, surface diffusion was responsible for the start of the deformation, [36, 35] which resulted in stress propagating from the surface to the interior and facilitating internal point defects to evolve into stacking faults, accompanied by local melting as suggested by Link *et al.* [33] Then, the high strain around stacking faults caused a transformation into multiple twin structures. On the other hand, although observed in, [37] surface melting did not happen prior to the occurrence of planar defects. A plausible reason for the discrepancy is that the common neighbor analysis used in [37] ignores thermal displacement of the atoms (Figure S5) that can easily cause inaccuracies in detecting point defects of HCP structures at high temperatures. Although extended twin and double twin boundaries were observed to be almost free from atomic displacements compared to an ideal FCC lattice, [43] the ideal thermodynamic minimum corresponds to a single-crystalline FCC structure. For laser-heated NRs, the heating and cooling rates are too fast to allow reorganization into a single crystalline lattice. With enough time at higher temperatures and during cooling, the Au NR will strive to-

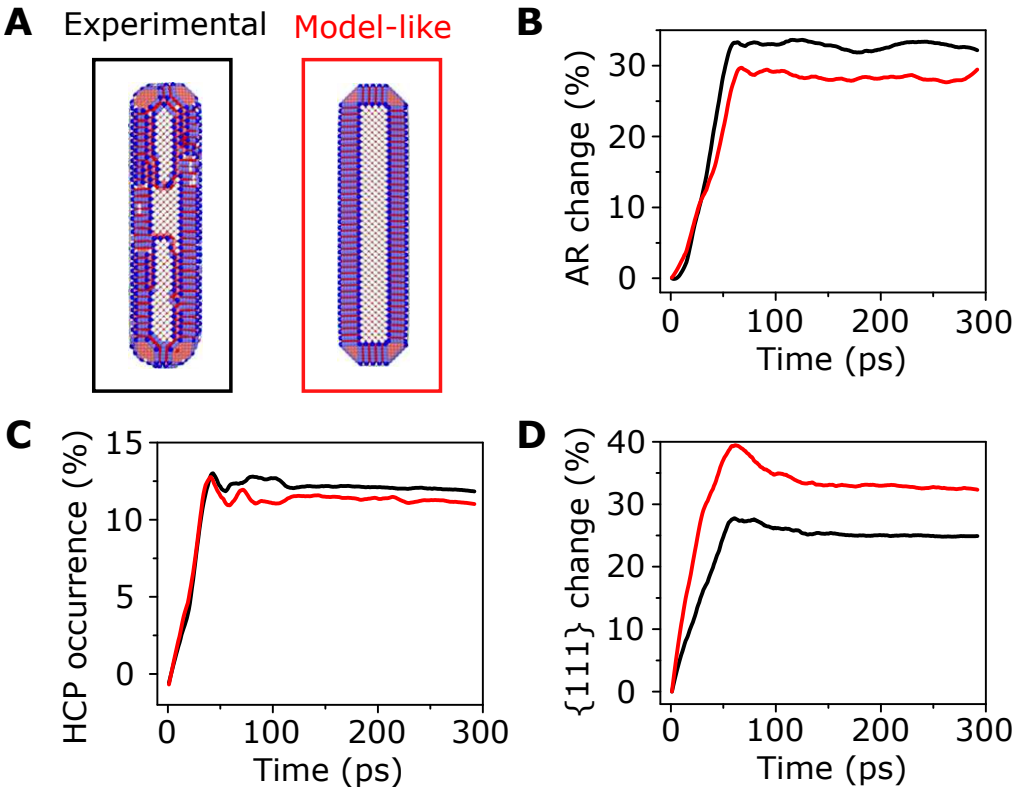

Figure 6: Comparison of MD results for the model-like (red curves) and experimental-based (black curves) input structure A). Shown are the B) AR change, C) HCP occurrence and D) relative change in {111} facets.

wards eliminating the internal defects resulting in NRs with reduced twin boundaries (Figure 1D, S9 and S19).

Our results thus show that laser-induced deformation is a complex process defined by a delicate interplay between thermodynamics and kinetics. The actual kinetic pathway of the transformation is difficult to predict and a controversy exists between curvature-driven, [16] defect-driven [33] and facet-driven [36, 35] below-melting-point deformation. By performing slow heating experiments inside the TEM, it was proposed that the shape determines the kinetic pathway. [44] Whereas for NRs, curvature was the dominant factor with reshaping to rounder shapes with higher index facets, deformation of triangular nanoplates was driven by surface faceting. Indeed, in our case the NP's tips became more rounded indicating curvature-driven surface diffusion. However, the changes in surface facets can only be quantified based on 3D information as done here. The change in morphology actually allows for an increase of stable {111} surface facets and decrease of more unstable facets. Despite having the same curvature with the NR from the experimental input, the facets of the model-like NR were found to change more, reducing the overall energy. Thus, curvature and facet-driven below-melting-point deformation are not necessarily competing processes but are rather intertwined.

The amount of facet transformation was indeed linked to the initial facet distribution and the same initial AR and volume of the NR did not result in the same deformation dynamics (Figure S13B and Figure 6). This becomes clear from the comparison of the model-like NR with the morphology based on experiments. In the latter case, the amount of stable {111} facets was higher but yet it deformed more. This can be explained by the fact that the initial surface disorder present for the experimental NR influenced the deformation dynamics, providing kinks and steps on the side of the NR as a low-energy path for atoms diffusing from the tips. On the contrary, the nucleation of new atomic planes was necessary for diffusing atoms for the model-like structure, [45] leading to an increase in stability. This will not only depend on the amount of disorder but also on the exact ratio of initial facets.

Deeper knowledge over reshaping and restructuring is tremendously important for the routine use of silica-coated metal NPs in actual applications. For this purpose, our results provide an understanding concerning the conditions under which defects are formed and reshaping occurs. For most plasmonic ap-

plications such as imaging, sensing and biomedicine, reshaping and atomic restructuring is unwanted because it changes the carefully designed optical properties. Moreover, the creation of even a single lattice defect already causes plasmon broadening. [46] Our work demonstrates that local temperatures of more than 1000 K can be achieved for silica-coated Au NRs without inducing structural and morphological modifications, which is not possible for bare Au NRs. Furthermore, we would like to particularly highlight the importance of controlled restructuring for catalytic applications. It was recently demonstrated that a high density of stacking faults in Ag NPs immensely increased the activity for the hydrogen evolution reaction, thereby outperforming conventional Pt catalysts. [47] Being able to control the internal restructuring as well as occurrence of specific surface facets will be a powerful tool in future catalytic research. [48] As shown in our work, a mesoporous silica coating gives a significantly better control over the density of stacking faults, strain and surface coordination numbers compared to bare Au NPs. Our work paves the way towards tuning these parameters by changing the amount of absorbed heat (either by changing the aspect ratio of the NP or excitation power) to create highly active and stable future catalysts.

To conclude, by combining experimentally retrieved 3D atomic scale information and MD simulations, we have shown that fs laser-induced deformation with energies below the melting point proceeds twofold: 1) the NR deforms towards its thermodynamic equilibrium shape by curvature-driven surface diffusion and 2) the nanocrystal additionally lowers its free energy by creating more low-energy surface facets at the cost of internal twin boundaries. The latter are induced by a combination of atomic strain and localized melting. To reproduce the experimental data, we included the cooling process in the simulations. By doing so, we observed that a mesoporous silica coating did not only stabilize Au NRs upon laser heating but also influenced the structure after deformation, which is due to the combination of a modified cooling profile and hindrance of surface diffusion. Finally, we demonstrated that subtleties in atomic-scale morphology can significantly influence the physical properties of nanomaterials and their transformation mechanisms. Hence, the actual experimental morphology needs to be considered when studying dynamic atomistic processes. Therefore, incorporating realistic morphologies in models and simulations will be imperative for understanding and predicting the behavior of nanomaterials in practically relevant conditions. We expect that the methodology and insights demonstrated in the present study will be valuable for open questions such as the effect of atomic distribution and crystal defects in nanoparticles on their optical properties and catalytic performance.

Experimental Section

For details see sections 'Experimental methods' and 'Computational methods' in the Supporting Information.

Synthesis of silica-coated gold nanorods: A modified version of Ye *et al.*was used to synthesis gold nanorods. [49] A 18 nm mesoporous silica shell was grown via the method of Gorelikov *et al.*. [50] All details can be found in the section 'Synthesis of mesoporous silica-coated Au NRs' in the Supporting Information.

Femtosecond laser excitation: A Leica SP8 confocal setup (63x/1.4 oil-immersion objective) equipped with a Coherent Chameleon II Ti:Sapphire laser (80 MHz repetition rate, 140 fs laser pulses). For the excitation, the on a TEM grid deposited NRs were immersed in glycerol and placed in-between two glass slides. The excitation wavelength was 925 nm and 860 nm for the small and large nanorods, respectively. The wavelength was chosen according to the ensemble-averaged longitudinal plasmon resonance of the corresponding sample on a glass slide and immersed in glycerol. All details can be found in the section 'Femtosecond laser excitation' in the Supporting Information.

Transmission electron microscopy: BF-TEM images were acquired using a TECNAI12 electron microscope, whereas HAADF-STEM images and electron tomography tilt series were acquired using an aberration corrected 'cubed' FEI-Titan electron microscope, operated at 300 kV. Atomic resolution series of the nanorod before and after laser excitation were acquired within a tilt range from -69 °to +72 °with a tilt increment of 3 °and 2 °, respectively. After distortion corrections with the help of a convolutional

neural network, 3D reconstructions were performed by the Simultaneous Iterative Reconstruction Technique (SIRT) and the application of constraints in real and Fourier space, following our previous work. [51] The acquisition and reconstruction procedures differed slightly for the series before and after laser excitation. All details are in the Supporting Information.

Molecular dynamics simulations: For the MD simulations, two different input models were created: model-like single crystalline gold nanorods with different ARs and an input structure based on the atomic resolution tomography before laser excitation. All created input structures had a diameter of 4 nm. Details can be found in section 'Creating input models' in the Supporting Information. The mesoporous silica coating was simulated by creating a silica aerogel based on the study of Patil *et al.*. [41] All structures were relaxed before the start of the simulation. A femtosecond heating profile was applied according to Baffou et al. [52] and the Lumped capacitance method for the heat dissipation [53] which are detailed in section 'Heating regime of the femtosecond laser simulations' in the Supporting Information. All the molecular dynamics (MD) simulations were carried out in the NVT ensemble using the program Large-scale Atomic/Molecular Massively Parallel Simulator (LAMMPS). [54] The equations of motion were integrated using the velocity Verlet algorithm with a time step of 1 fs. Periodic boundary conditions were applied in all three directions with a large vacuum area. 'Force matching' of the embedded atom model (EAM) [55] was used for the interaction between Au atoms and the inter-atomic potential of Vashishta *et al.* for the silica gel. [56] For the interaction between the Au atoms and the mesoporous silica coating, a Lennard-Jones potential was applied. The change in surface facets, the internal structure and the atomic strain analysis of the Au nanorods under laser irradiation were qualitatively and quantitatively analyzed by the OVITO open visualization tool and OVITO Python open-source scripts. [57] Extended details of all simulation steps can be found in the Supporting Information.

Supporting Information
Supporting Information is available from the Wiley Online Library or from the author.

Acknowledgements
W.A. and E.A.I. contributed equally to this work. The authors acknowledge funding from the European Research Council under the European Union's Horizon 2020 research and innovation program (ERC Consolidator Grants No. 815128 - REALNANO and No. 770887 - PICOMETRICS and ERC Advanced Grant No. 291667 - HierarSACol) and the European Commission (EUSMI). W.A. acknowledges an Individual Fellowship funded by the Marie Sklodowska-Curie Actions (MSCA) in Horizon 2020 program (grant 797153, SOPMEN). T.S.D. acknowledges financial support from the National Science Foundation of China (NSFC, Grant no. 61905056). The authors also acknowledge financial support by the Research Foundation Flanders (FWO grant G.0267.18N).

References

[1] E. C. Dreaden, A. M. Alkilany, X. Huang, C. J. Murphy, M. A. El-Sayed, *Chem. Soc. Rev.* **2012**, *41* 2740.

[2] W. Q. Lim, Z. Gao, *Nano Today* **2016**, *11* 168.

[3] A. G. Brolo, *Nat. Photonics* **2012**, *6* 709.

[4] M. Li, S. K. Cushing, N. Wu, *Analyst* **2015**, *140* 386.

[5] M. I. Stockman, *Science* **2015**, *348* 287.

[6] P.-C. Li, S.-W. Huang, C.-W. Wei, Y.-C. Chiou, C.-D. Chen, C.-R. C. Wang, *Opt. Lett.* **2005**, *30* 3341.

[7] P.-C. Li, C.-R. C. Wang, D.-B. Shieh, C.-W. Wei, C.-K. Liao, C. Poe, S. Jhan, A.-A. Ding, Y.-N. Wu, *Opt. Express* **2008**, *16* 18605.

[8] P. Zijlstra, J. W. M. Chon, M. Gu, *Nature* **2009**, *459* 410.

[9] A. B. Taylor, J. Kim, J. W. M. Chon, *Opt. Express* **2012**, *20* 5069.

[10] Q. Dai, M. Ouyang, W. Yuan, J. Li, B. Guo, S. Lan, S. Liu, Q. Zhang, G. Lu, S. Tie, H. Deng, Y. Xu, M. Gu, *Adv. Mater.* **2017**, *29* 1701918.

[11] S. Linic, U. Aslam, C. Boerigter, M. Morabito, *Nat. Mater.* **2015**, *14* 567.

[12] U. Aslam, V. G. Rao, S. Chavez, S. Linic, *Nat. Catal.* **2018**, *1* 656.

[13] Z. Zhang, C. Zhang, H. Zheng, H. Xu, *Acc. Chem. Res.* **2019**, *52* 2506.

[14] S. Link, C. Burda, B. Nikoobakht, M. A. El-Sayed, *J. Phys. Chem. B* **2000**, *104* 6152.

[15] P. Zijlstra, J. W. M. Chon, M. Gu, *Phys. Chem. Chem. Phys.* **2009**, *11* 5915.

[16] A. B. Taylor, A. M. Siddiquee, J. W. M. Chon, *ACS Nano* **2014**, *8* 12071.

[17] J. Yan, D. Zhu, J. Xie, Y. Shao, W. Xiao, *Small* **2020**, *16* 2001101.

[18] S. Link, C. Burda, M. B. Mohamed, B. Nikoobakht, M. A. El-Sayed, *J. Phys. Chem. A* **1999**, *103* 1165.

[19] Y.-S. Chen, W. Frey, S. Kim, K. Homan, P. Kruizinga, K. Sokolov, S. Emelianov, *Opt. Express* **2010**, *18* 8867.

[20] P. Zijlstra, J. W. M. Chon, M. Gu, *Opt. Express* **2007**, *15* 12151.

[21] Y. Horiguchi, K. Honda, Y. Kato, N. Nakashima, Y. Niidome, *Langmuir* **2008**, *24* 12026.

[22] W. Albrecht, T.-S. Deng, B. Goris, M. A. van Huis, S. Bals, A. van Blaaderen, *Nano Lett.* **2016**, *16* 1818.

[23] S. C. Nguyen, Q. Zhang, K. Manthiram, X. Ye, J. P. Lomont, C. B. Harris, H. Weller, A. P. Alivisatos, *ACS Nano* **2016**, *10*, 2 2144.

[24] G. González-Rubio, P. Díaz-Núñez, A. Rivera, A. Prada, G. Tardajos, J. González-Izquierdo, L. Bañares, P. Llombart, L. G. Macdowell, M. A. Palafox, L. M. Liz-Marzán, O. Peña-Rodríguez, A. Guerrero-Martínez, *Science* **2017**, *358* 640.

[25] F. Della Picca, M. V. Gutiérrez, A. V. Bragas, A. F. Scarpettini, *J. Phys. Chem. C* **2018**, *122* 29598.

[26] C. Graf, D. Vossen, A. Imhof, A. van Blaaderen, *Langmuir* **2003**, *19* 6693.

[27] C. Hanske, M. N. Sanz-Ortiz, L. M. Liz-Marzán, *Adv. Mater.* **2018**, *30* 1707003.

[28] Z. Zhang, L. Wang, J. Wang, X. Jiang, X. Li, Z. Hu, Y. Ji, X. Wu, C. Chen, *Adv. Mater.* **2012**, *24* 1418.

[29] Y.-S. Chen, W. Frey, S. Kim, P. Kruizinga, K. Homan, S. Emelianov, *Nano Lett.* **2011**, *11* 348.

[30] P. Zijlstra, J. W. Chon, , M. Gu, *Optics Express* **2007**, *15* 12151.

[31] S. H. Joo, J. Y. Park, C.-K. Tsung, Y. Yamada, P. Yang, G. A. Somorjai, *Nature Materials* **2009**, *8* 126.

[32] J.-N. Park, A. J. Forman, W. Tang, J. Cheng, Y.-S. Hu, H. Lin, E. W. McFarland, *Small* **2008**, *4* 1694.

[33] S. Link, Z. L. Wang, M. A. El-Sayed, *J. Phys. Chem. B* **2000**, *104* 7867.

[34] N. Sumimoto, K. Nakao, T. Yamamoto, K. Yasuda, S. Matsumura, Y. Niidome, *Microscopy* **2014**, *63* 261.

[35] G. Opletal, G. Grochola, Y. H. Chui, I. K. Snook, S. P. Russo, *J. Phys. Chem. C* **2011**, *115* 4375.

[36] Y. Wang, S. Teitel, C. Dellago, *Nano Lett.* **2005**, *5* 2174.

[37] Y. Gan, S. Jiang, *J. Appl. Phys.* **2013**, *113* 073507.

[38] K. Aso, K. Shigematsu, T. Yamamoto, S. Matsumura, *Microscopy* **2019**, *68* 174.

[39] G. González-Rubio, J. González-Izquierdo, L. Bañares, G. Tardajos, A. Rivera, T. Altantzis, S. Bals, O. Peña-Rodríguez, A. Guerrero-Martínez, L. M. Liz-Marzán, *Nano Lett.* **2015**, *15* 8282.

[40] H. Petrova, J. Perez Juste, I. Pastoriza-Santos, G. V. Hartland, L. M. Liz-Marzán, P. Mulvaney, *Phys. Chem. Chem. Phys.* **2006**, *8* 814.

[41] S. P. Patil, A. Rege, Sagardas, M. Itskov, B. Markert, *J. Phys. Chem. B* **2017**, *121* 5660.

[42] L. D. Marks, L. Peng, *J. Phys. Condens. Matter* **2016**, *28* 053001.

[43] K. Aso, K. Shigematsu, T. Yamamoto, S. Matsumura, *Microscopy* **2016**, *65* 391.

[44] H. Cho, J. W. Shin, R. Ryoo, *J. Phys. Chem. C* **2020**, *124* 12855.

[45] N. Combe, P. Jensen, A. Pimpinelli, *Phys. Rev. Lett.* **2000**, *85* 110.

[46] T. Milagres de Oliveira, W. Albrecht, G. González-Rubio, T. Altantzis, I. P. Lobato Hoyos, A. Béché, S. Van Aert, A. Guerrero-Martínez, L. M. Liz-Marzán, S. Bals, *ACS Nano* **2020**, *14* 12558.

[47] Z. Li, J.-Y. Fu, Y. Feng, C.-K. Dong, H. Liu, X.-W. Du, *Nat. Catal.* **2019**, *2* 1107.

[48] J. van der Hoeven, J. Jelic, L. Olthof, G. Totarella, R. J. A. van Dijk-Moes, F. Studt, A. V. Blaaderen, P. E. de Jongh **2020**, *10.26434/chemrxiv.13218155.v1.*

[49] X. Ye, C. Zheng, J. Chen, Y. Gao, C. B. Murray, *Nano Lett.* **2013**, *13* 765.

[50] I. Gorelikov, N. Matsuura, *Nano Lett.* **2008**, *8* 369.

[51] T. Altantzis, I. Lobato, A. De Backer, A. Béché, Y. Zhang, S. Basak, M. Porcu, Q. Xu, A. Sánchez-Iglesias, L. M. Liz-Marzán, G. Van Tendeloo, S. Van Aert, S. Bals, *Nano Lett.* **2019**, *19* 477.

[52] G. Baffou, *Thermoplasmonics: Heating Metal Nanoparticles Using Light*, Cambridge University Press, **2017**.

[53] F. P. Incropera, *Fundamentals of Heat and Mass Transfer*, John Wiley & Sons, Inc., Hoboken, NJ, USA, **2011**.

[54] S. Plimpton, *J. Comput. Phys.* **1995**, *117* 1.

[55] G. Grochola, S. P. Russo, I. K. Snook, *J. Chem. Phys.* **2005**, *123* 204719.

[56] P. Vashishta, A. Nakano, R. K. Kalia, I. Ebbsjö, *J. Non-Cryst. Solids* **1995**, *182* 59 .

[57] A. Stukowski, *Modelling Simul. Mater. Sci. Eng.* **2012**, *20* 045021.

Table of Contents

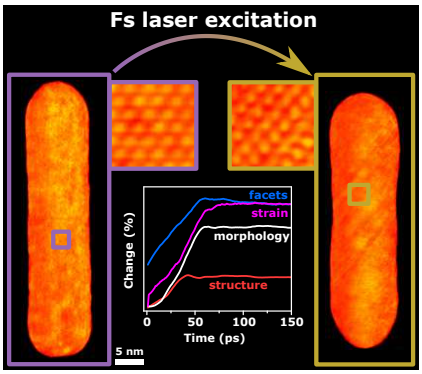

Atomic resolution electron tomography reveals atomic rearrangements in metal nanoparticles upon femtosecond laser excitation. Based on the measured three-dimensional atomic structure, molecular dynamics simulations unravel the dynamics of the underlying process and give insight how strain, crystal facet distribution and surface diffusion govern these rearrangements.